Nano Research

Open Access

Research Article

Industrial-grade electrocatalytic valorization of waste plastics via reconstructed Ni^{2+}-CoOOH nanosheet arrays

Jinxuan Wu[1], Jinfeng Zheng[2], Zhouhong Yu[1], Cong Lin[1], Kun Chen[1], Nan Zhang[3] ✉, and Pengzuo Chen[1] ✉

[1] *School of Chemistry and Chemical Engineering, Zhejiang Sci-Tech University, Hangzhou 310018, China*
[2] *Key Laboratory of Graphene Forestry Application of National Forest and Grass Administration, Engineering Research Center of Coal-based Ecological Carbon Sequestration Technology of the Minstry of Education, Shanxi Datong University, Datong 037009, China*
[3] *State Key Laboratory of Green Chemical Engineering and Industrial Catalysis, Sinopec, Shanghai Research Institute of Petrochemical Technology Co., Ltd., Shanghai 201208, China*

Cite this article: *Nano Research*, **2025**, *18*, 94907806. https://doi.org/10.26599/NR.2025.94907806

ABSTRACT: Electrocatalytic upcycling of polyethylene terephthalate (PET) waste plastics into value-added chemicals offers a promising strategy to address environmental pollution. However, the development of efficient electrocatalysts capable of operating under industrial-level current densities remains a significant challenge. In this study, we report an electrochemical reconstruction strategy to fabricate Ni^{2+}-doped CoOOH nanosheet arrays directly on nickel foam (NF), enabling highly efficient conversion of PET-derived ethylene glycol (EG) into formate at high current densities. Systematic investigations, including *in situ* spectroscopic analysis, reveal that Ni^{2+} doping not only enhances the adsorption of EG molecules on the catalyst surface but also accelerates the formation of reactive *OH intermediates, thereby improving the reaction kinetics of C–C bond cleavage, ultimately promoting efficient formate production. Specifically, the optimized Ni^{2+}-$CoOOH_3$/NF catalyst achieves an industrial-level current density of 500 mA·cm^{-2} at an ultralow potential of 1.38 V vs. RHE, with a Faradaic efficiency exceeding 90% across a broad current density range of 100–500 mA·cm^{-2}. Furthermore, in a practical two-electrode electrolyzer, the Ni^{2+}-$CoOOH_3$/NF delivers a high formate yield of 7.10 mmol·h^{-1}·cm^{-2} at 900 mA·cm^{-2}, along with excellent long-term operational stability.

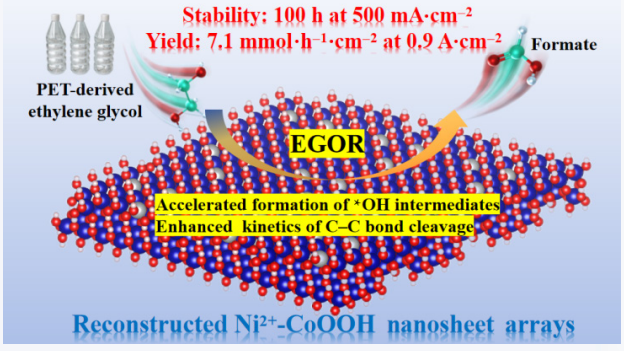

KEYWORDS: Ni^{2+}-CoOOH nanosheet, industrial-grade performance, electrochemical reconstruction, polyethylene terephthalate (PET) waste plastic, formate product

1 Introduction

The improper disposal of plastic waste-particularly its accumulation in landfills and migration into aquatic environments has caused escalating ecological and environmental concerns [1, 2]. Among various types of plastics, polyethylene terephthalate (PET) accounts for over 82 million tons of annual production, predominantly used in packaging and textiles [3]. Traditional recycling strategies for PET, including mechanical reprocessing and pyrolysis, are hindered by low efficiency and environmental limitations [4]. Recently, the electrochemical upcycling of PET waste under mild conditions offers a sustainable and efficient alternative [5–7]. In an alkaline medium, PET can be hydrolyzed into terephthalic acid (TPA) and ethylene glycol (EG). Among these, EG is electrochemically oxidizable into formate (FA), a high-value product widely used in fuel cells, chemical synthesis, and industrial processes [8]. Importantly, FA features high economic value and environmental compatibility. Electrochemical oxidation of EG (EGOR) achieves selective C–C bond cleavage at the anode, with product selectivity largely governed by the adsorption configuration of intermediates and the energy barrier of bond dissociation [9–11]. Therefore, the development of high-performance electrocatalysts capable of achieving both high activity and stability under large current densities is critical to realizing the practical implementation of electrocatalytic PET upgrading technologies.

In recent years, cobalt-based catalysts, especially those in the form of oxides and hydroxides, have shown great promise in

Received: May 31, 2025; **Revised:** July 4, 2025
Accepted: July 15, 2025

✉Address correspondence to Pengzuo Chen, pzchen0421@126.com; Nan Zhang, zhangn.sshy@sinopec.com

EGOR applications due to their earth abundance, moderate binding energies for reaction intermediates, and favorable redox characteristics [12–15]. However, their catalytic performance remains limited by the linear adsorption behavior of active sites, which constrains reaction kinetics and selectivity. To address these challenges, numerous studies have focused on enhancing activity of cobalt-based catalysts via strategies such as heteroatom doping, heterostructure engineering, and alloying [16–18]. Metal doping, in particular, has been demonstrated to improve both the intrinsic activity and formate selectivity of cobalt-based materials [19]. Nonetheless, systems capable of sustaining long-term operation at industrial current densities remain scarce. Fundamentally, the key to controlling EGOR selectivity and efficiency lies in the adsorption kinetics and electronic structure modulation of key reaction intermediates, especially reactive oxygen species such as *OH [20]. The *OH intermediate plays a pivotal role in facilitating C–C bond cleavage, dehydrogenation, and product coupling [21]. Therefore, engineering the surface and interfacial structure of cobalt-based catalysts to accelerate *OH generation and its subsequent oxidation kinetics is one of the most promising strategies for enhancing industrial EGOR performance.

Herein, we present a rationally designed Ni^{2+}-doped CoOOH nanosheet catalyst, synthesized via electrodeposition and electrochemical reconstruction, for the efficient electrooxidation of EG derived from PET hydrolysate. The incorporation of Ni^{2+} significantly enhances the generation of reactive *OH species and improves the adsorption and conversion kinetics of EG, thereby promoting the selective cleavage of C–C bonds to form formate. Comprehensive *in situ* spectroscopic analyses and electrochemical measurements confirm that the optimized Ni^{2+}-$CoOOH_3$/NF catalyst delivers industrial-level performance, achieving 500 $mA{\cdot}cm^{-2}$ at a low potential of 1.38 V vs. RHE and maintaining over 90% Faradaic efficiency (FE) across a wide current range. When integrated into a two-electrode HER||EGOR electrolyzer, the system co-produces formate and hydrogen with outstanding stability, reaching a formate yield of 7.10 $mmol{\cdot}h^{-1}{\cdot}cm^{-2}$ at 900 $mA{\cdot}cm^{-2}$. The successful recovery of high-purity terephthalic acid and potassium formate further demonstrates the practical applicability of this approach.

2 Result and discussion

In this study, the Ni^{2+}-$Co(OH)_2$/NF electrode was first synthesized via a one-step electrodeposition method. Subsequently, a selective electrochemical activation and reconstruction process was employed to convert Ni^{2+}-$Co(OH)_2$/NF into the final Ni^{2+}-CoOOH/NF material, as schematically illustrated in Fig. 1(a). The phase compositions of the synthesized materials were investigated using X-ray diffraction (XRD). As shown in Fig. S1 in the ESM, the XRD patterns of both Ni^{2+}-$Co(OH)_2$ and $Co(OH)_2$ display several characteristic peaks corresponding to the standard $Co(OH)_2$ phase (JCPDS card No. 45-0031). After electrochemical reconstruction, the XRD pattern of Ni^{2+}-CoOOH is consistent with the standard CoOOH phase (JCPDS card No. 26-0480), as shown in Fig. S2 in the ESM, indicating the successful transformation from Ni^{2+}-$Co(OH)_2$ to Ni^{2+}-CoOOH.

The surface morphology and microstructure of the samples were further characterized by scanning electron microscopy (SEM). As depicted in Figs. S3 and S4 in the ESM, both Ni^{2+}-$Co(OH)_2$/NF and Ni^{2+}-CoOOH/NF exhibit nanosheet arrays uniformly grown on the three-dimensional (3D) porous nickel foam substrate, confirming the successful construction of integrated electrode architectures. The Ni^{2+}-CoOOH/NF possesses a thinner nanosheet morphology compared to the Ni^{2+}-$Co(OH)_2$/NF, indicating that electrochemical reconstruction optimizes the material's active surface to form two-dimensional flakes with more exposed active sites. Transmission electron microscopy (TEM) in Fig. 1(b) further reveals the thin nanosheet property of Ni^{2+}-CoOOH, while high-resolution TEM (HRTEM) identifies lattice fringes with an interplanar spacing of 0.220 nm, corresponding to the (004) plane of CoOOH (Fig. 1(c)). Energy-dispersive X-ray spectroscopy (EDS) elemental mapping (Fig. 1(d)) confirms the uniform distribution of Co, Ni, and O throughout the nanosheet structure. In addition, X-ray photoelectron spectroscopy (XPS) was conducted to analyze the surface chemical states of Ni^{2+}-$Co(OH)_2$/NF and Ni^{2+}-CoOOH/NF. In the high-resolution Co 2p spectra (Fig. S5 in the ESM), Ni^{2+}-$Co(OH)_2$/NF displays peaks at binding energies of 781.2 and 796.9 eV, corresponding to Co^{2+} $2p_{3/2}$ and Co^{2+} $2p_{1/2}$, along with satellite features at 786.2 and 802.9 eV [22]. After reconstruction, Ni^{2+}-CoOOH/NF exhibits distinct Co^{3+} $2p_{3/2}$ (780.1 eV) and Co^{3+} $2p_{1/2}$ (795.2 eV) peaks, confirming the formation of CoOOH [23]. Notably, the high-resolution Ni 2p spectra of both samples (Fig. S6 in the ESM) only show peaks attributable to Ni^{2+} species, suggesting that the Ni^{2+} are successfully doping into CoOOH and its valence state remains unchanged throughout the reconstruction process [24].

To further corroborate these observations, X-ray absorption fine structure (XAFS) measurements were carried out for Ni^{2+}-$Co(OH)_2$, Ni^{2+}-CoOOH, $Co(OH)_2$, and CoOOH samples. As shown in Fig. 1(e) and Fig. S7 in the ESM, Co K-edge X-ray absorption near-edge structure (XANES) spectra reveal a positive shift in the absorption edge for Ni^{2+}-CoOOH and CoOOH compared to Ni^{2+}-$Co(OH)_2$ and $Co(OH)_2$, indicating the oxidation of Co^{2+} to Co^{3+} during reconstruction. Furthermore, the extended X-ray absorption fine structure (EXAFS) spectra in Fig. S7(a) in the ESM reveal comparable oscillatory features between Ni^{2+}-CoOOH and CoOOH, indicating that the electrochemical reconstruction successfully induced the structural transformation from $Co(OH)_2$ to CoOOH. Notably, the Ni K-edge XANES spectra (Fig. 1(f)) and EXAFS spectra (Fig. S7(b) in the ESM) exhibit consistent spectral characteristics for both Ni^{2+}-$Co(OH)_2$ and Ni^{2+}-CoOOH. These spectral similarities suggest that the valence state and local coordination environment of Ni remain largely preserved during the electrocatalytic reconstruction process, which is also consistent with the XPS results. Fourier transform (FT) EXAFS analysis was also conducted to explore the local coordination environment. In Fig. 1(g), Ni^{2+}-$Co(OH)_2$ and $Co(OH)_2$ exhibit two prominent peaks at approximately ~ 1.45 and ~ 2.69 Å, corresponding to Co–O and Co–Co/Ni coordination, respectively. In contrast, Ni^{2+}-CoOOH and CoOOH show shifts in coordination peaks, indicative of significant structural evolution. For the Ni K-edge FT-EXAFS spectra (Fig. 1(h)), two peaks centered at ~ 1.53 and ~2.65 Å are assigned to Ni–O and Ni–Co/Ni coordination. Compared to Ni^{2+}-$Co(OH)_2$, the lower intensity of the Ni–Co/Ni peak in Ni^{2+}-CoOOH suggests increased structural disorder post-reconstruction. Furthermore, wavelet transform (WT) EXAFS spectra of both the Co and Ni K-edges (Figs. 1(i) and 1(j) and Fig. S8 in the ESM) provide additional evidence of the distinct coordination environments and successful directional transformation from Ni^{2+}-$Co(OH)_2$ to Ni^{2+}-CoOOH. These results collectively confirm the successful and controllable

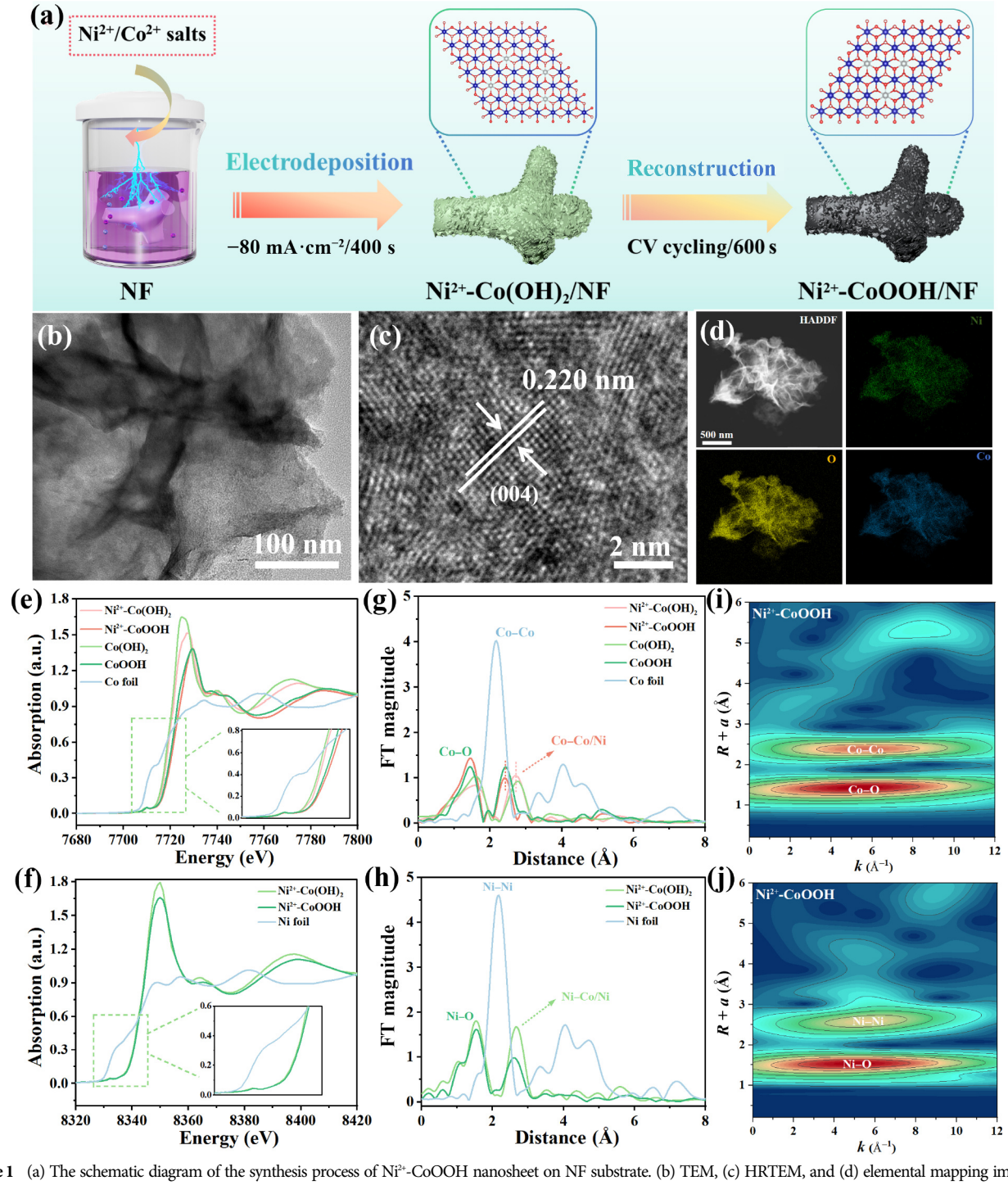

Figure 1 (a) The schematic diagram of the synthesis process of Ni^{2+}-CoOOH nanosheet on NF substrate. (b) TEM, (c) HRTEM, and (d) elemental mapping images of Ni^{2+}-CoOOH sample. The XANES spectra of (e) Co K-edge and (f) Ni K-edge and FT-EXAFS spectra of (g) Co K-edge and (h) Ni K-edge for the references and prepared samples. (i) and (j) Wavelet transforms for the k^2-weighted EXAFS spectra of Ni^{2+}-CoOOH.

synthesis of Ni^{2+}-CoOOH/NF electrodes via an electrochemical reconstruction strategy.

The electrocatalytic performance of the Ni^{2+}-CoOOH/NF and the other control catalysts for the EGOR were systematically evaluated in a homemade PET hydrolysate solution. As shown in Fig. 2(a), the linear sweep voltammetry (LSV) curve recorded in the PET hydrolysate exhibited significantly enhanced catalytic activity compared to that in 1.0 M KOH electrolyte. Remarkably, the Ni^{2+}-CoOOH/NF electrode required an ultra-low potential of just 1.38 V vs. RHE to reach a current density of 500 mA·cm^{-2}, representing a substantial about 220 mV reduction in overpotential relative to the oxygen evolution reaction (OER). Furthermore, this performance surpasses that of control catalysts that synthsized by using different ratios of Ni/Co sources, including Ni^{2+}-$CoOOH_1$/NF (1.55 V vs. RHE), Ni^{2+}-$CoOOH_2$/NF (1.44 V vs. RHE), Ni^{2+}-$CoOOH_4$/NF (1.48 V vs. RHE), and undoped CoOOH/NF (1.62 V vs. RHE) (Fig. 2(b) and Fig. S9(a) in the ESM), demonstrating the critical role of Ni^{2+} doping and the optimal Ni/Co ratio (1:4) in enhancing

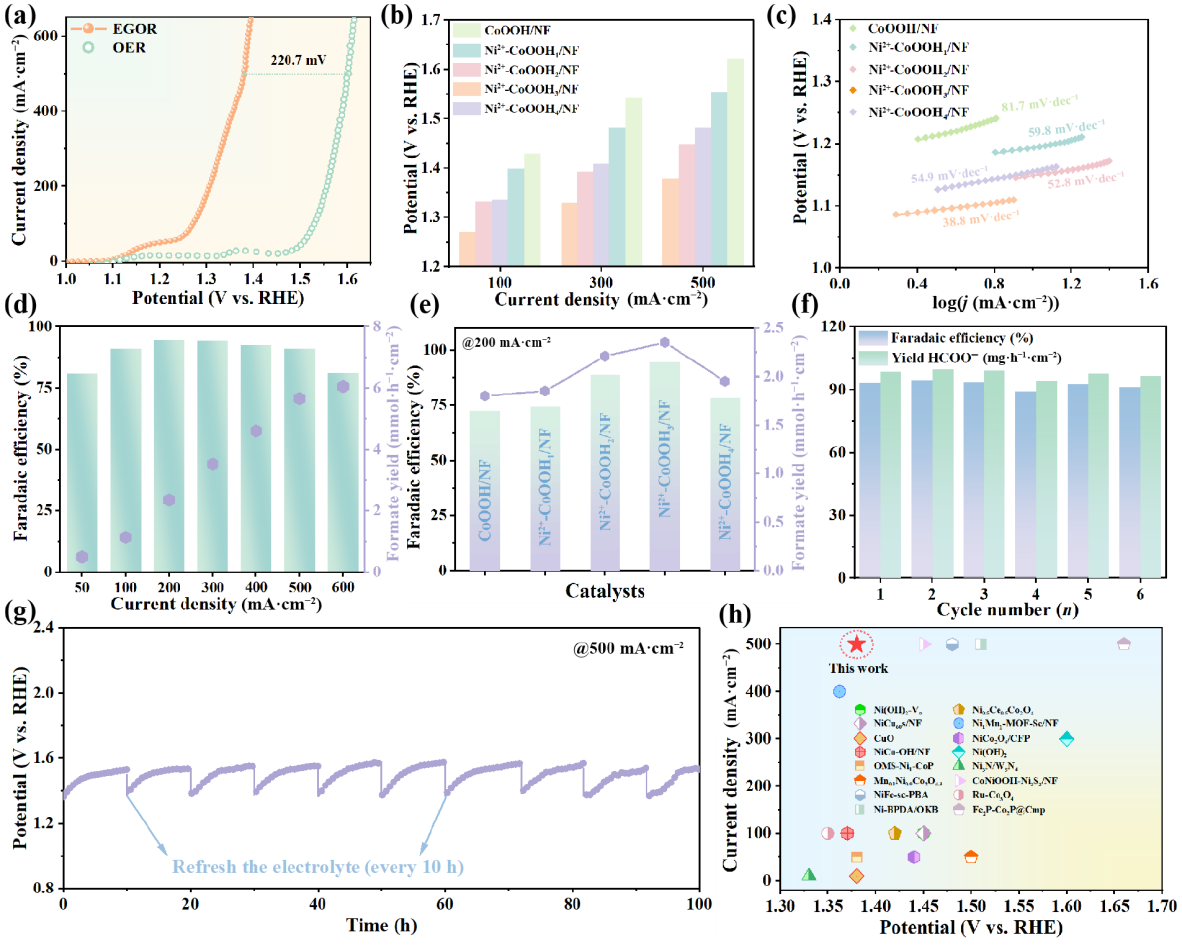

Figure 2 (a) LSV curves for Ni^{2+}-$CoOOH_3$/NF in PET hydrolysate and 1 M KOH. (b) Potential comparison diagrams at different current densities and (c) Tafel slopes for the prepared catalysts in PET hydrolysate. (d) FE and formate yield of Ni^{2+}-$CoOOH_3$/NF at different current densities. (e) The comparison of yields and FEs of formate among those prepared catalysts at 200 mA·cm^{-2}. (f) The cycling tests and (g) stability test of Ni^{2+}-$CoOOH_3$/NF for EGOR at 500 mA·cm^{-2}. (h) Performance comparison of Ni^{2+}-$CoOOH_3$/NF with the other reported catalysts for EGOR.

EGOR activity. Meanwhile, the Tafel slope of Ni^{2+}-$CoOOH_3$/NF was calculated to be as low as 38.8 mV·dec^{-1}, which is also lower than that of Ni^{2+}-$CoOOH_1$/NF (59.8 mV·dec^{-1}), Ni^{2+}-$CoOOH_2$/NF (52.8 mV·dec^{-1}), Ni^{2+}-$CoOOH_4$/NF (54.9 mV·dec^{-1}), and CoOOH/NF (81.7 mV·dec^{-1}), indicating the optimized EGOR kinetics (Fig. 2(c)). This result is further supported by electrochemical impedance spectroscopy (EIS), where Ni^{2+}-$CoOOH_3$/NF exhibits the smallest charge-transfer resistance among all tested catalysts (Fig. S9(b) in the ESM) [25–30].

To evaluate the electrochemical surface properties, the double-layer capacitance (C_{dl}) values were derived from cyclic voltammetry (CV) measurements at various scan rates (Fig. S10 in the ESM). Ni^{2+}-$CoOOH_3$/NF exhibited the highest C_{dl} value of 3.1 mF·cm^{-2}, outperforming Ni^{2+}-$CoOOH_1$/NF (2.3 mF·cm^{-2}), Ni^{2+}-$CoOOH_2$/NF (2.7 mF·cm^{-2}), Ni^{2+}-$CoOOH_4$/NF (2.8 mF·cm^{-2}), and CoOOH/NF (1.7 mF·cm^{-2}), suggesting a larger electrochemically active surface area and the availability of more accessible active sites (Fig. S11 in the ESM) [31–36]. To confirm the intrinsic activity, the EGOR current densities were normalized to the electrochemical surface area (ECSA), and the Ni^{2+}-$CoOOH_3$/NF electrode consistently exhibited the highest intrinsic activity across all samples (Fig. S12 in the ESM), further verifying that the superior catalytic performance stems not only from the increased surface area but also from enhanced intrinsic properties [27].

The EGOR products generated under different current densities were identified and quantified by ^{1}H nuclear magnetic resonance (NMR) spectroscopy. As shown in Fig. S13 in the ESM, characteristic peaks corresponding to maleic acid (MA), TPA, residual EG, and the target product formate were clearly observed. The Ni^{2+}-$CoOOH_3$/NF electrode achieved a FE of over 90% across the current density range of 100–500 mA·cm^{-2}, with a maximum FE of 94.5% at 200 mA·cm^{-2}. Additionally, a high formate yield of 6.05 mmol·h^{-1}·cm^{-2} was obtained at 600 mA·cm^{-2} (Fig. 2(d)). These results significantly outperform the performance of control catalysts, such as CoOOH/NF (72.4%, 1.80 mmol·h^{-1}·cm^{-2}), Ni^{2+}-$CoOOH_1$/NF (74.4%, 1.85 mmol·h^{-1}·cm^{-2}), Ni^{2+}-$CoOOH_2$/NF (88.8%, 2.20 mmol·h^{-1}·cm^{-2}), and Ni^{2+}-$CoOOH_4$/NF (78.4%, 1.95 mmol·h^{-1}·cm^{-2}) (Fig. 2(e)), further validating the superior catalytic capability of the Ni^{2+}-$CoOOH_3$/NF electrode for EGOR. Moreover, long-term electrolysis tests demonstrated excellent durability. As shown in Figs. 2(f) and 2(g), the Ni^{2+}-$CoOOH_3$/NF catalyst maintained a stable cell voltage and consistent formate FE over 100 h of continuous operation at 500 mA·cm^{-2}, confirming its outstanding operational stability and potential for practical applications in biomass-derived electrosynthesis systems. It is worth mentioning that the Ni^{2+}-$CoOOH_3$/NF catalyst achieved industrial current density (500 mA·cm^{-2}) at a much lower potential than other reported PET electrocatalytic upgrade materials (Fig. 2(h) and Table S1 in the ESM).

In addition, a series of post-mortem characterizations have further been performed on the Ni^{2+}-$CoOOH_3$/NF catalyst after the 20-hour long-term EGOR test to investigate any structural or compositional changes. As shown in Fig. S14 in the ESM, the XRD patterns of the used catalyst display no discernible phase changes compared to the fresh sample, indicating that the crystalline structure remains stable. Furthermore, SEM images confirm that the nanosheet morphology is well-preserved after prolonged electrolysis, with no significant aggregation or collapse observed. Additionally, XPS analysis shows that the oxidation states of Co and Ni remain consistent before and after the reaction, suggesting that the surface chemical environment and electronic structure of the active sites are maintained. These results collectively confirm the excellent structural and electrochemical stability of the Ni^{2+}-$CoOOH_3$/NF catalyst under extended reaction conditions.

To further elucidate the mechanistic origin of the enhanced electrocatalytic performance of the Ni^{2+}-$CoOOH_3$/NF electrode in EGOR, *in situ* EIS was employed to probe the kinetic characteristics at the electrode-electrolyte interface. As shown in the Bode phase plot for OER (Fig. 3(a)), Ni^{2+}-$CoOOH_3$/NF exhibits a characteristic phase peak in the low-frequency region at 1.45 V vs. RHE. In contrast, during EGOR, the corresponding phase peak emerges at a significantly lower potential of 1.20 V vs. RHE (Fig. 3(b)), indicating that EGOR proceeds with faster interfacial kinetics than OER [37]. Compared with the CoOOH/NF electrode, where the phase peak appears at 1.40 V vs. RHE (Fig. S15 in the ESM), the Ni^{2+}-doped catalyst demonstrates a noticeable reduction in peak potential, confirming that Ni^{2+} doping effectively promotes EGOR kinetics and accelerates the transformation of ethylene glycol into formate [38]. The emergence of the phase peak during EGOR can be attributed to a non-uniform charge distribution arising from the oxidation of EG molecules on the catalyst surface, which reflects a dynamic charge redistribution process at the interface [39]. Notably, the EGOR phase peak occurs in a similar low-frequency region as the OER, suggesting a mechanistic correlation with adsorbed hydroxyl (*OH) intermediates. As the applied potential increases, the peak shifts toward higher frequencies and lower phase angles, signifying faster charge transfer and accelerated oxidation of EG molecules [40]. This phenomenon is more pronounced in Ni^{2+}-$CoOOH_3$/NF compared to CoOOH/NF, highlighting the promoting role of Ni^{2+} doping in interfacial charge dynamics.

To further investigate the adsorption behavior of EG on different catalysts, open-circuit potential (OCP) measurements were conducted to evaluate the adsorption capacity within the inner Helmholtz layer. As shown in Fig. 3(c), both Ni^{2+}-$CoOOH_3$/NF and CoOOH/NF exhibit a marked decrease in OCP upon the introduction of EG. Notably, Ni^{2+}-$CoOOH_3$/NF shows a greater shift, indicating a stronger adsorption of EG molecules, which facilitates surface reaction initiation [41]. In addition, based on previous literature, alcohol electrooxidation performance is closely associated with both the adsorption strength of reactants and the generation efficiency of surface-active *OH species [42, 43]. LSV

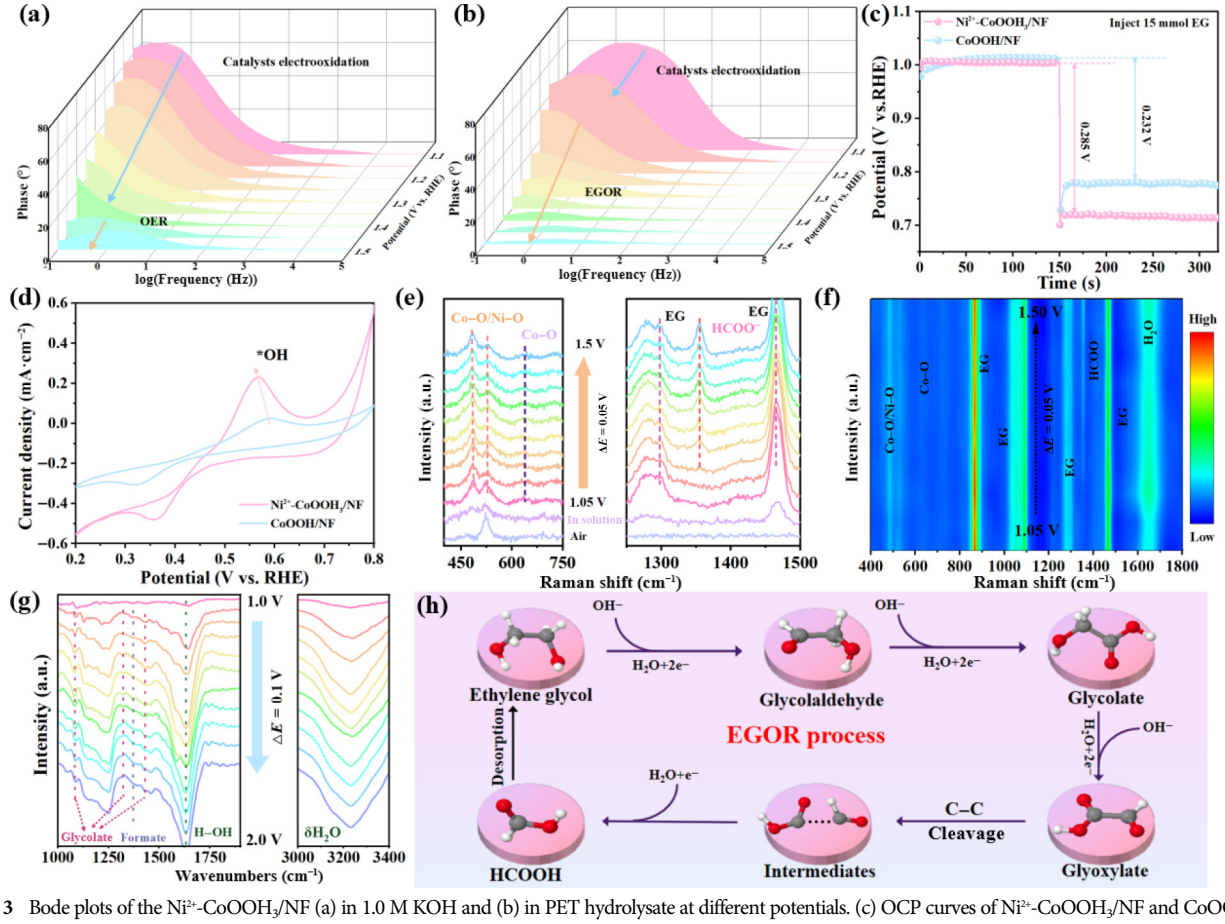

Figure 3 Bode plots of the Ni^{2+}-$CoOOH_3$/NF (a) in 1.0 M KOH and (b) in PET hydrolysate at different potentials. (c) OCP curves of Ni^{2+}-$CoOOH_3$/NF and CoOOH/NF with and without adding EG in 1.0 M KOH solution. (d) CV curves of Ni^{2+}-$CoOOH_3$/NF and CoOOH/NF in 1.0 M KOH solution. (e) The intercepted characteristic peaks and (f) contour maps of *in situ* Raman spectroscopy for the Ni^{2+}-$CoOOH_3$/NF during EGOR test. (g) The *operando* FTIR spectra of Ni^{2+}-$CoOOH_3$/NF for EGOR. (h) The proposed conversion pathway of EGOR to formate on Ni^{2+}-$CoOOH_3$/NF.

curves (Fig. 3(d)) reveal that Ni^{2+}-$CoOOH_3$/NF exhibits a more intense *OH formation peak around 0.6 V vs. RHE compared to CoOOH/NF, further suggesting that Ni^{2+} doping enhances the generation of reactive oxygen species and optimizes the subsequent oxidation kinetics of EG molecules. Therefore, the incorporation of Ni^{2+} into the CoOOH nanosheets plays multiple beneficial roles in enhancing EGOR performance. Firstly, the heteroatomic Ni^{2+} sites likely serve as additional catalytic centers to facilitate the adsorption and activation of ethylene glycol molecules. Secondly, Ni^{2+} doping may enhance the generation of reactive *OH species by accelerating water dissociation kinetics, which is a crucial step for alcohol oxidation reactions. Thirdly, the integration of Ni^{2+} into the CoOOH lattice introduces electronic modulation effects that can alter the local charge distribution. This results in the formation of asymmetric Ni^{2+}–Co^{3+} bimetallic active sites, which may promote synergistic catalytic behavior and lower the energy barrier for key bond-breaking steps in the EGOR pathway.

To provide direct insight into surface species during EGOR, *in situ* Raman spectroscopy was performed. As shown in Figs. 3(e) and 3(f), the peaks located at 481, 520, and 642 cm^{-1} in the 400–750 cm^{-1} range are attributed to Co–O/Ni–O vibrational modes and lattice vibrations of Co–O in the Ni^{2+}-$CoOOH_3$/NF [40, 44]. With increasing potential, the intensities of these peaks increase, while no additional peaks emerge, indicating that the CoOOH phase remains the primary active component throughout the EGOR process. In the higher Raman region, broad peaks at 1280 and 1468 cm^{-1} correspond to the vibrational signals of the EG reactant, whereas a distinct peak at 1353 cm^{-1} is associated with the formate product [45]. Complementary *in situ* Fourier-transform infrared (FTIR) spectroscopy was conducted to trace the evolution of intermediate species. As shown in Fig. 3(g), with increasing potential, the characteristic absorption bands at 1080, 1320, and 1411 cm^{-1} can be assigned to the aldehyde stretching vibration, C–O stretching vibration, and symmetric $–COO^-$ stretching of glycolic acid, respectively [46]. The appearance of a new band at 1380 cm^{-1} confirms the formation of formate [47]. Compared to CoOOH/NF (Fig. S16 in the ESM), Ni^{2+}-$CoOOH_3$/NF exhibits stronger absorption intensities for both intermediates and final products, highlighting its improved activity toward EGOR to formate. Based on these findings, the proposed EGOR pathway is illustrated in Fig. 3(h). Initially, EG molecules are electrochemically oxidized on the Ni^{2+}-$CoOOH_3$/NF catalyst surface to form glycolic acid intermediates. Subsequently, C–C bond cleavage occurs, generating formate as the final oxidation product [48]. This mechanistic understanding underscores the critical role of Ni^{2+} doping and interfacial charge redistribution in enhancing the catalytic efficiency of Ni^{2+}-$CoOOH_3$/NF during biomass-derived electrooxidation processes.

Based on the above results, Ni^{2+}-$CoOOH_3$/NF has been demonstrated to exhibit exceptional electrocatalytic performance for the continuous conversion of PET hydrolysate into formate under industrial-level current densities. The energy-saving water splitting for hydrogen generation is considered as a promising hybrid technology [49–54]. To further evaluate its practical applicability in an overall water electrolysis system, we constructed a two-electrode cell pairing Ni^{2+}-$CoOOH_3$/NF as the anode with a highly efficient hydrogen evolution reaction (HER) catalyst, $MoNi_4$@MoO_2/NF, as the cathode (Fig. 4(a) and Fig. S17 in the ESM) [54]. This configuration enabled a coupled HER||EGOR electrolyzer. First, LSV was performed to compare the energy efficiency of a conventional HER||OER electrolyzer and the HER||EGOR electrolyzer. As shown in Fig. 4(b) and Fig. S18 in the ESM, at a current density of 1000 $mA·cm^{-2}$, the HER||EGOR electrolyzer required only 2.16 V, nearly 462 mV lower than that of the HER||OER counterpart. This significant voltage reduction highlights the energy-saving advantage of replacing the sluggish OER with the kinetically favorable EGOR process. Hydrogen generated at the cathode was collected via the water displacement method [55–61], while the formate produced at the anode was quantitatively analyzed using ^1H NMR spectroscopy.

As shown in Fig. 4(c), the HER||EGOR electrolyzer achieved a formate Faradaic efficiency exceeding 90% over a wide current density range (100–500 $mA·cm^{-2}$). Notably, at an industrially relevant current density of 900 $mA·cm^{-2}$, the formate yield reached an impressive 7.10 $mmol·h^{-1}·cm^{-2}$. Even at 500 $mA·cm^{-2}$, the system maintained a high formate Faradaic efficiency (91.5%), significantly outperforming many state-of-the-art electrocatalytic systems previously reported (Fig. 4(e) and Table S2 in the ESM), thereby confirming the superior catalytic performance of the designed electrolyzer. In addition, the hydrogen production rate under various coulombic charge inputs closely matched the theoretical values (Fig. 4(d)), further validating the high hydrogen Faradaic efficiency of the system. To assess the long-term operational stability and industrial viability, the HER||EGOR electrolyzer was operated continuously at 500 $mA·cm^{-2}$ for 100 h. As shown in Fig. 4(f), the cell voltage remained stable throughout the entire electrolysis period, and the formate production rate was consistently maintained, demonstrating excellent durability and scalability for sustained co-production of hydrogen and formate. Finally, the anodic oxidation products were collected and subjected to downstream purification via concentration and recrystallization techniques (Fig. S19 in the ESM). XRD analysis confirmed the successful isolation of high-purity potassium formate (HCOOK) and TPA as solid products (Fig. 4(g)). Additionally, to further evaluate the practicality of this electrochemical PET-to-formate strategy, a comprehensive economic analysis is shown in Fig. S20 and Table S3 in the ESM according to the presented calculation details in the ESM, the process yields an estimated economic benefit of $235.27 per ton of PET waste, which strongly supports the commercial viability of this technology for upcycling plastic waste into high-value chemicals.

3 Conclusions

In summary, a Ni^{2+}-doped CoOOH/NF electrocatalyst featuring a hierarchical nanosheet morphology was successfully synthesized via a facile electrodeposition followed by electrochemical reconstruction strategy. Comprehensive physicochemical characterizations confirmed the synergistically optimized active sites and interfacial charge transfer capability. *In situ* spectroscopic analysis further revealed that Ni^{2+} doping promotes the formation of reactive *OH species, enhances the adsorption of ethylene glycol molecules, and facilitates the generation of key reaction intermediates, thereby accelerating the overall kinetics of EG-to-formate conversion. Electrochemical performance evaluation demonstrated that the optimized Ni^{2+}-CoOOH/NF electrode exhibits industrial-level catalytic activity in a three-electrode system. When integrated into a two-electrode HER||EGOR electrolyzer, the device delivered superior co-electrolysis performance for the anodic formate and cathodic H_2 products. Moreover, the purified products,

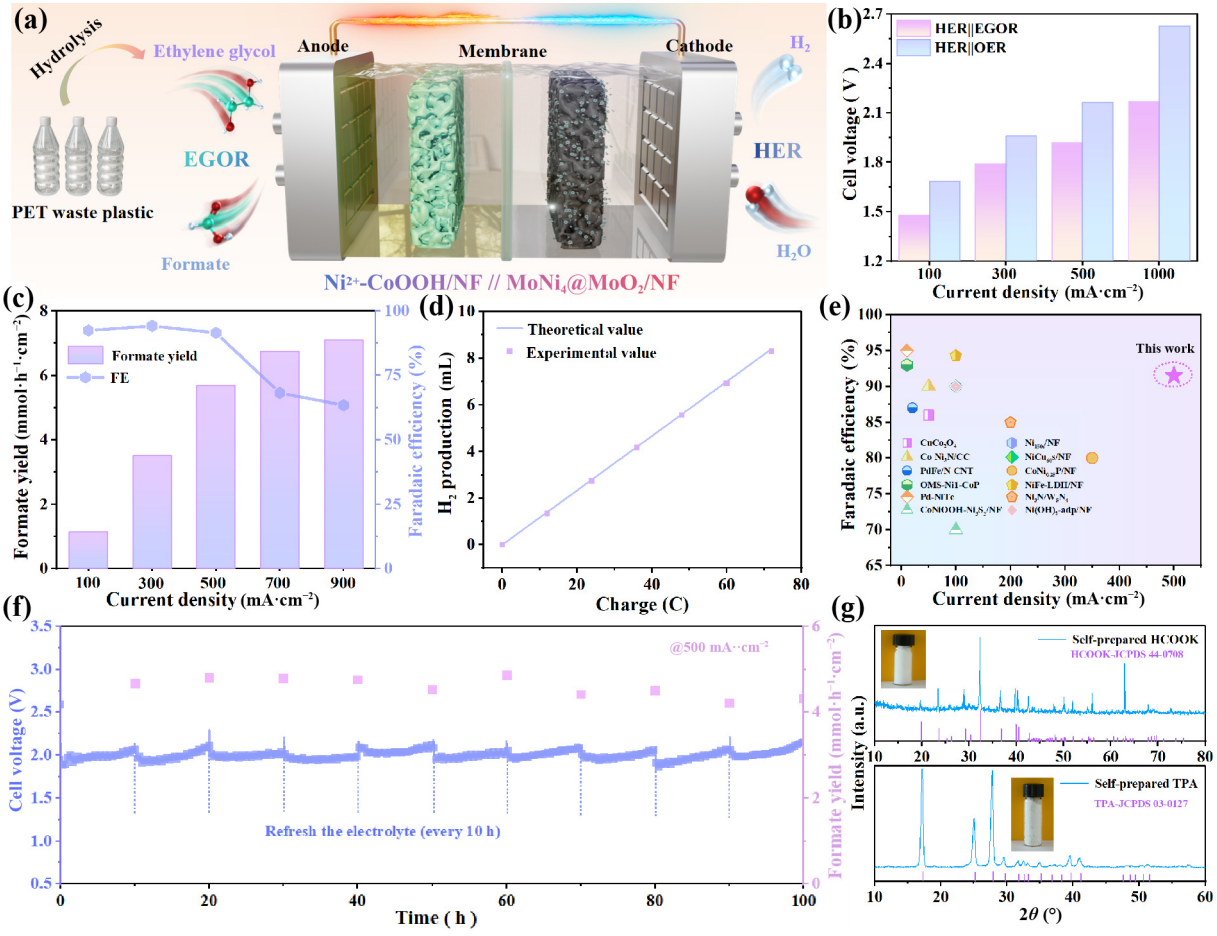

Figure 4 (a) Schematic diagram of MEA electrolyzer. (b) Volatge comparison of the HER||EGOR and HER||OER electrolyzers at different current densities. (c) The FE and yield of anodic formate at different current densities. (d) The cathodic yield of H_2 at different coulombic charge. (e) The performance comparison with the other electrolyzers by using different catalysts. (f) Chronopotentiometry test of HER||EGOR electrolyzer at 500 mA·cm^{-2}. (g) XRD patterns and pictures of purified potassium formate and isolated terephthalic acid products.

TPA and HCOOK, were successfully recovered after the continuous electrolysis, confirming the feasibility of this strategy for efficient upcycling of PET waste into high-value chemicals and fuels.

4 Methods section

4.1 Synthesis of a series of Ni^{2+}-CoOOH/NF samples

The Ni^{2+}-$CoOOH_3$/NF samples were prepared by electrodeposition and electrochemical reconstruction method. Typically, the cleaned nickel foam was used as working electrode in a traditional three-electrode system and the electrolyte consists of 5 mmol $Co(NO_3)_2{\cdot}6H_2O$ and 1.25 mmol $Ni(NO_3)_2{\cdot}6H_2O$ in 50 mL of distilled water. A continuous current of −80 mA·cm^{-2} was applied to the working electrode for 400 s to prepare the Ni^{2+}-$Co(OH)_2$/NF sample. Next, the electrochemical reconstruction was performed by using the Ni^{2+}-$Co(OH)_2$/NF as working electrode in PET hydrolysate and conducted at the potential range of 0–1 V via cyclic voltammetry cycling tests for 600 s. The Ni^{2+}-$CoOOH_3$/NF electrode was washed with water to remove the absorbed electrolyte and dried in a vacuum oven. Moreover, by only adjusting the ratios of $Co(NO_3)_2{\cdot}6H_2O$ and $Ni(NO_3)_2{\cdot}6H_2O$ (2.5, 3.75, 6.25 mmol: 1.25 mmol) in the electrolytes, the Ni^{2+}-$CoOOH_1$/NF, Ni^{2+}-$CoOOH_2$/NF, and Ni^{2+}-$CoOOH_4$/NF can be synthesized. The CoOOH/NF electrode was prepared by only using single Co source under the same conditions.

4.2 Synthesis of $MoNi_4@MoO_2$/NF samples

Firstly, $NiMoO_4$ precursor was prepared by hydrothermal reaction. The 1 cm × 2 cm nanofiltration membrane was cleaned with 3 M hydrochloric acid solution, deionized water, and anhydrous ethanol for 15 min to remove surface oxidation layer and impurities. Then, 0.47 g nickel nitrate hexahydrate ($Ni(NO_3)_2{\cdot}6H_2O$) and 0.5 g ammonium molybdate tetrahydrate ($(NH_4)_6Mo_7O_{24}{\cdot}6H_2O$) were added into 60 mL deionized water and stirred for 30 min to obtain a uniform solution. Then, the above solution and one NF were transferred to a 100 mL stainless steel reactor, and the reaction was maintained at 150 °C for 6 h. The $NiMoO_4$ precursor was removed and washed three times with deionized water and anhydrous ethanol. The $NiMoO_4$ precursor was placed in the furnace with flowing H_2/N_2 mixture atmosphere, and was annealed for 1 h at the temperature of 500 °C. After cooling to room temperature, the final $MoNi_4@MoO_2$ material was obtained.

4.3 The preparation of PET hydrolysate

20 g of PET powder (polyethylene terephthalate) was placed in 100 mL of potassium hydroxide solution (KOH, 2.5 M) and stirred

in a water bath at 80 °C for 90 h. The PET hydrolysate was then filtered and adjusted to 500 mL for the electrochemical tests.

The other detailed experimental sections have already shown in the ESM.

Electronic Supplementary Material: Supplementary material (experimental details, the XRD patterns, XPS spectra, SEM images, XAFS spectra, ^{1}H NMR spectra, Tables, and other electrochemical result) is available in the online version of this article at https://doi.org/10.26599/NR.2025.94907806.

Data availability

All data needed to support the conclusions in the paper are presented in the manuscript and the Electronic Supplementary Material. Additional data related to this paper may be requested from the corresponding author upon request.

Acknowledgements

This work is financially supported by the Fundamental Research Funds of Zhejiang Sci-Tech University (ZSTU) (No. 25262157-Y). We also thank SCI-GO (https://www.sci-go.com) for the SEM measurement. The authors thank the staff of beamline BL11B and BL13SSW at Shanghai Synchrotron Radiation Facility for experiments supports.

Declaration of competing interest

No known competing financial interests need to be declared.

Author contribution statement

J. X. W., J. F. Z., and Z. H. Y.: Data curation, project administration. C. L. and K. C.: Validation, experimental design, software. N. Z. and P. Z. C.: Funding acquisition, writing manuscript, supervisor. All the authors have approved the final manuscript.

Use of AI statement

None.

References

[1] Hu, Q. Y.; Zhang, Z. X.; He, D. P.; Wu, J. C.; Ding, J. Y.; Chen, Q. X.; Jiao, X. C.; Xie, Y. Progress and perspective for "green" strategies of catalytic plastics conversion into fuels by regulating half-reactions. *J. Am. Chem. Soc.* **2024**, *146*, 16950–16962.

[2] Qin, J. B.; Wu, F. Y.; Dou, Y. B.; Zhao, D.; Hélix-Nielsen, C.; Zhang, W. J. Advanced catalysts for the chemical recycling of plastic waste. *Adv. Mater.* **2025**, *37*, 2418138.

[3] Han, S.; Sun, L. Z.; Fan, D. P.; Liu, B. Pulsed electrosynthesis of glycolic acid through polyethylene terephthalate upcycling over a mesoporous PdCu catalyst. *Nat. Commun.* **2025**, *16*, 3426.

[4] Bharadwaj, C.; Purbey, R.; Bora, D.; Chetia, P.; Maheswari R, U.; Duarah, R.; Dutta, K.; Sadiku, E. R.; Varaprasad, K.; Jayaramudu, J. A review on sustainable PET recycling: Strategies and trends. *Mater. Today Sustain.* **2024**, *27*, 100936.

[5] Ding, W.; Ji, D. X.; Wang, K. K.; Li, Y. H.; Luo, Q. L.; Wang, R. W.; Li, L. L.; Qin, X. H.; Peng, S. J. Rapid surface reconstruction of amorphous-crystalline NiO for industrial-scale electrocatalytic PET upcycling. *Angew. Chem., Int. Ed.* **2025**, *64*, e202418640.

[6] Wang, J. Y.; Li, X.; Wang, M. L.; Zhang, T.; Chai, X. Y.; Lu, J. L.; Wang, T. F.; Zhao, Y. X.; Ma, D. Electrocatalytic valorization of poly(ethylene terephthalate) plastic and CO_2 for simultaneous production of formic acid. *ACS Catal.* **2022**, *12*, 6722–6728.

[7] Du, D. F.; Liu, P. X.; Teng, Z. Q.; Chen, T. Y.; Zhu, J.; Shao, B.; Luo, J. S. Ampere-level upgrading of polyethylene terephthalate to glycolate using palladium-copper/nickel hydroxide electrocatalysts. *ACS Catal.* **2025**, *15*, 3038–3045.

[8] Du, D. F.; Kang, F. S.; Yang, S. R.; Shao, B.; Luo, J. S. Co-electrolysis of ethylene glycol and carbon dioxide for formate synthesis. *Sci. China Chem.* **2024**, *67*, 1539–1544.

[9] Li, J. S.; Li, L. M.; Ma, X. Y.; Han, X.; Xing, C. C.; Qi, X. Q.; He, R.; Arbiol, J.; Pan, H. Y.; Zhao, J. et al. Selective ethylene glycol oxidation to formate on nickel selenide with simultaneous evolution of hydrogen. *Adv. Sci.* **2023**, *10*, 2300841.

[10] Zhang, J. S.; Zhang, X. L.; Shi, C.; Yu, X. Y.; Zhou, Y. T.; Di, L. B. Plasma-constructed Co_2P–Ni_2P heterointerface for electro-upcycling of polyethylene terephthalate plastic to Co-produce hydrogen and formate. *Small* **2024**, *20*, 2406767.

[11] Zhang, H. G.; Wang, Y. L.; Li, X. M.; Deng, K.; Yu, H. J.; Xu, Y.; Wang, H. J.; Wang, Z. Q.; Wang, L. Electrocatalytic upcycling of polyethylene terephthalate plastic to formic acid coupled with energy-saving hydrogen production over hierarchical Pd-doped NiTe nanoarrays. *Appl. Catal. B: Environ.* **2024**, *340*, 123236.

[12] Niu, Z. D.; Fan, S. Y.; Li, X. Y.; Chen, G. H. Electrocatalytic Co-upcycling of nitrite and ethylene glycol over cobalt-copper oxides. *Adv. Energy Mater.* **2024**, *14*, 2303515.

[13] Liu, F. L.; Gao, X. T.; Shi, R.; Tse, E. C. M.; Chen, Y. A general electrochemical strategy for upcycling polyester plastics into added-value chemicals by a $CuCo_2O_4$ catalyst. *Green Chem.* **2022**, *24*, 6571–6577.

[14] Xu, G. R.; Dong, Z. M.; Zhao, Y. X.; Zhang, W.; Sun, Q. Y.; Ju, D. X.; Wang, L. Alkali etching of porous PdCoZn nanosheets for boosting C–C bond cleavage of ethylene glycol oxidation. *Small* **2024**, *20*, 2306341.

[15] Wang, Y. F.; Luo, X.; Lu, W. J.; Huang, B.; Yang, Y. Q. RhCo alloyed nanodendrites as an efficient electrocatalyst for boosting electro oxidation of ethylene glycol in alkaline media. *Chem. Eng. J.* **2024**, *499*, 155924.

[16] Jiang, J. D.; Zhang, L. T.; Wu, G. Z.; Zhang, J. R.; Yang, Y. D.; He, W. H.; Zhu, J.; Zhang, J.; Qin, Q. Efficient electrochemical-enzymatic conversion of PET to formate coupled with nitrate reduction over Ru-doped Co_3O_4 catalysts. *Angew. Chem., Int. Ed.* **2025**, *64*, e202421240.

[17] Wu, J. X.; Cheng, X. X.; Tong, Y.; Yu, Z. H.; Lin, C.; Zhang, N.; Chen, L.; Chen, P. Z. Interface engineering on heterostructural nanosheets for efficient electrocatalytic-paired upcycling of waste plastics and nitrate. *ACS Catal.* **2024**, *14*, 18095–18106.

[18] Ren, T. L.; Duan, Z. Y.; Wang, H. Z.; Yu, H. J.; Deng, K.; Wang, Z. Q.; Wang, H. J.; Wang, L.; Xu, Y. Electrochemical co-production of ammonia and biodegradable polymer monomer glycolic acid via the co-electrolysis of nitrate wastewater and waste plastic. *ACS Catal.* **2023**, *13*, 10394–10404.

[19] Ren, T. L.; Yu, Z.; Yu, H. J.; Deng, K.; Wang, Z. Q.; Li, X. N.; Wang, H. J.; Wang, L.; Xu, Y. Sustainable ammonia electrosynthesis from nitrate wastewater coupled to electrocatalytic upcycling of polyethylene terephthalate plastic waste. *ACS Nano* **2023**, *17*, 12422–12432.

[20] Sun, J. Y.; Shi, B. K.; Dai, S. X.; Chu, L.; Wang, H. L.; Huang, M. H. Promoted *OH adsorption facilitates C–C bond cleavage for efficient electrochemical upcycling of polyethylene terephthalate. *ACS Catal.* **2025**, *15*, 529–542.

[21] Liang, C. J.; Zhao, R. Y.; Chen, T.; Luo, Y.; Hu, J. Q.; Qi, P.; Ding, W. P. Recent approaches for cleaving the C–C bond during ethanol electro-oxidation reaction. *Adv. Sci.* **2024**, *11*, 2308958.

[22] Zhao, X. Y.; Long, M.; Li, Z. X.; Zhang, Z. H. A two dimensional

$Co(OH)_2$ catalytic gravity-driven membrane for water purification: A green and facile fabrication strategy and excellent water decontamination performance. *Mater. Horiz.* **2024**, *11*, 1435–1447.

[23] Zhou, P. Y.; Pan, H. K.; Hai, G. T.; Liu, X.; Huang, X. B.; Wang, G. Expediting *OH accumulation kinetics on metal-organic frameworks-derived CoOOH with CeO_2 "accelerator" for electrocatalytic 5-hydroxymethylfurfural oxidation valorization. *J. Energy Chem.* **2024**, *98*, 721–732.

[24] Shi, X. Y.; Xie, M. H.; Yang, K. W.; Niu, Y. T.; Ma, H. B.; Zhu, Y. M.; Li, J. Y.; Pan, T. T.; Zhou, X. Y.; Cui, Y. J. et al. Synergistic effect of $Ni/Ni(OH)_2$ core–shell catalyst boosts tandem nitrate reduction for ampere-level ammonia production. *Angew. Chem., Int. Ed.* **2024**, *63*, e202406750.

[25] Zhu, J. Y.; Zhou, G. R.; Tong, Y.; Chen, L.; Chen, P. Z. Vanadium oxide clusters mediated bismuth-tin alloy for accelerated dynamics of electrocatalytic CO_2 conversion. *Adv. Funct. Mater.* **2025**, *35*, 2420177.

[26] Wang, M. D.; Chen, P. Z.; Wang, H. G.; Zhao, Y. Y. Heterogeneous β-$Co(OH)_2/Cu_2(OH)_3Cl$ bifunctional electrocatalyst for superior concurrent conversion of glycerol and nitrite. *J. Energy Chem.* **2025**, *104*, 185–193.

[27] Zhou, G. R.; Cheng, H.; Wu, Y. L.; Tong, Y.; Dai, R. H.; Zhu, J. Y.; Zheng, X. N.; Lin, C.; Chen, P. Z.; Wu, C. Z. Industrial-level paired electrosynthesis of valuable chemicals over a high-performance heterostructural electrode. *Angew. Chem., Int. Ed.* **2025**, *64*, e202420353.

[28] Yu, Z. H.; Chen, K.; Tong, Y.; Lin, C.; Zheng, X. N.; Chen, P. Z. Phosphorus-modulated cobalt nanosheets with confined metal defects for enhanced kinetics in nitrite-glycerol Co-electrolysis. *Adv. Funct. Mater.*, in press, https://doi.org/10.1002/adfm.202506735.

[29] Zhu, J. Y.; Luo, L.; Lai, C.; He, B.; Chen, P. Z. Confining bismuth in oxygen-defective $BiVO_4$ through chemical reconstruction engineering for enhanced electrocatalytic formate generation. *Chem. Eng. J.* **2025**, *517*, 164420.

[30] Jin, G. M.; Ren, X. H.; Lin, C.; He, B.; Chen, P. Z. Dual-metal heterogeneous electrode enabling efficient co-electrosynthesis of adipic acid and hydrogen. *J. Colloid Interface Sci.* **2025**, *687*, 432–438.

[31] Guo, Y. M.; Zhou, G. R.; Tong, Y. Electronic interaction of ruthenium species on bimetallic phosphide for superior electrocatalytic hydrogen generation. *Dalton Trans.* **2023**, *52*, 12733–12741.

[32] Tong, Y.; Chen, L.; Dyson, P. J.; Fei, Z. F. Boosting hydrogen production via urea electrolysis on an amorphous nickel phosphide/graphene hybrid structure. *J. Mater. Sci.* **2021**, *56*, 17709–17720.

[33] Feng, D. M.; Liu, X. Y.; Ye, R. Z.; Huang, W. X.; Tong, Y. Carbon-encapsulated Co_2P/P-modified $NiMoO_4$ hierarchical heterojunction as superior pH-universal electrocatalyst for hydrogen production. *J. Colloid Interface Sci.* **2023**, *634*, 693–702.

[34] Li, K. X.; Cen, X. J.; He, J. F.; Tong, Y. Coupled W-Co_2P hybrid nanosheets as a robust bifunctional electrocatalyst for hydrazine-assisted hydrogen production. *Chem. Commun.* **2023**, *59*, 5575–5578.

[35] Wang, H. J.; Cheng, X. X.; Tong, Y. Coupling of ruthenium with hybrid metal nitrides heterostructure as bifunctional electrocatalyst for water electrolysis. *J. Colloid Interface Sci.* **2023**, *629*, 155–164.

[36] Feng, D. M.; Zhang, S. S.; Tong, Y.; Dong, X. P. Dual-anions engineering of bimetallic oxides as highly active electrocatalyst for boosted overall water splitting. *J. Colloid Interface Sci.* **2022**, *623*, 467–475.

[37] Ge, R. X.; Wang, Y.; Li, Z. Z.; Xu, M.; Xu, S. M.; Zhou, H.; Ji, K. Y.; Chen, F. E.; Zhou, J. H.; Duan, H. H. Selective electrooxidation of biomass-derived alcohols to aldehydes in a neutral medium: Promoted water dissociation over a nickel-oxide-supported ruthenium single-atom catalyst. *Angew. Chem., Int. Ed.* **2022**, *61*, e202200211.

[38] Wang, H. Y.; Hung, S. F.; Chen, H. Y.; Chan, T. S.; Chen, H. M.; Liu, B. In *operando* identification of geometrical-site-dependent water oxidation activity of spinel Co_3O_4. *J. Am. Chem. Soc.* **2016**, *138*, 36–39.

[39] Chen, W.; Xie, C.; Wang, Y. Y.; Zou, Y. Q.; Dong, C. L.; Huang, Y. C.; Xiao, Z. H.; Wei, Z. X.; Du, S. Q.; Chen, C. et al. Activity origins and design principles of nickel-based catalysts for nucleophile electrooxidation. *Chem* **2020**, *6*, 2974–2993.

[40] Zhou, P.; Lv, X. S.; Tao, S. S.; Wu, J. C.; Wang, H. F.; Wei, X. X.; Wang, T. H.; Zhou, B.; Lu, Y. X.; Frauenheim, T. et al. Heterogeneous-interface-enhanced adsorption of organic and hydroxyl for biomass electrooxidation. *Adv. Mater.* **2022**, *34*, 2204089.

[41] Shi, K.; Si, D.; Teng, X.; Chen, L. S.; Shi, J. L. Pd/$NiMoO_4$/NF electrocatalysts for the efficient and ultra-stable synthesis and electrolyte-assisted extraction of glycolate. *Nat. Commun.* **2024**, *15*, 2899.

[42] Luo, H.; Wang, K.; Lin, F. X.; Lv, F.; Zhou, J. H.; Zhang, W. Y.; Wang, D. W.; Zhang, W. S.; Zhang, Q. H.; Gu, L. et al. Amorphous MoO_x with high oxophilicity interfaced with PtMo alloy nanoparticles boosts anti-CO hydrogen electrocatalysis. *Adv. Mater.* **2023**, *35*, 2211854.

[43] He, C. H.; Yan, Y. F.; Fu, Y.; Ma, C. Q.; Xia, J.; Han, S. M.; Zhang, H. F.; Ma, X.; Lin, G.; Feng, F. K. et al. Incorporating ordered indium sites into rhodium for ultra-low potential electrocatalytic conversion of ethylene glycol to glycolic acid. *Adv. Mater.* **2025**, *37*, 2418959.

[44] Lin, Y.; Chen, Y.; Ren, H.; Sun, Y. Y.; Chen, J. H.; Wu, M. B.; Li, Z. T. Inspiration of bimetallic peroxide for controllable electrooxidizing ethylene glycol through modulating surficial intermediates. *Adv. Funct. Mater.* **2024**, *34*, 2404594.

[45] Wu, J. X.; Liu, X.; Hao, Y. M.; Wang, S. Y.; Wang, R.; Du, W.; Cha, S. S.; Ma, X. Y.; Yang, X. J.; Gong, M. Ligand hybridization for electro-reforming waste glycerol into isolable oxalate and hydrogen. *Angew. Chem., Int. Ed.* **2023**, *62*, e202216083.

[46] Chang, S. C.; Ho, Y.; Weaver, M. J. Applications of real-time FTIR spectroscopy to the elucidation of complex electroorganic pathways: Electrooxidation of ethylene glycol on gold, platinum, and nickel in alkaline solution. *J. Am. Chem. Soc.* **1991**, *113*, 9506–9513.

[47] Zhou, G. R.; Zhang, N.; Huang, Z. H.; He, J. F.; Zhu, J. Y.; Ren, X. H.; Tong, Y.; Wang, H. G.; Chen, P. Z. Efficient paired electrolysis of glycerol upgrading with hydrogen fuel over heterostructured Fe-$Co_2Mo_3O_8$@Co electrocatalyst. *Chem. Eng. J.* **2025**, *503*, 158619.

[48] Wang, Z.; Li, J. H.; Zhang, Q.; Wu, C.; Meng, H. Y.; Tang, Y.; Zou, A. Q.; Zhang, Y. M.; Ma, R.; Lv, X. et al. Facilitating formate selectivity via optimizing e_g* band broadening in NiMn hydroxides for ethylene glycol electro-oxidation. *Angew. Chem., Int. Ed.* **2024**, *63*, e202411517.

[49] Zhu, S. C.; Yang, R. O.; Li, H. J. W.; Huang, S. R.; Wang, H. Z.; Liu, Y. W.; Li, H. Q.; Zhai, T. Y. Reconstructing hydrogen-bond network for efficient acidic oxygen evolution. *Angew. Chem., Int. Ed.* **2024**, *63*, e202319462.

[50] Lin, Y.; Huang, D. J.; Wen, Q. L.; Yang, R. O.; Chen, B. W.; Shen, Y.; Liu, Y. W.; Fang, J. K.; Li, H. Q.; Zhai, T. Y. Utilizing reconstruction achieves ultrastable water electrolysis. *Proc. Natl. Acad. Sci. USA* **2024**, *121*, e2407350121.

[51] Lin, Y.; Chen, B. W.; Huang, D. J.; Yang, Z. H.; Lu, A.; Shi, Z. Y.; Liu, Y. W.; Fang, J. K.; Li, H. Q.; Zhai, T. Y. Solid-liquid interfacial hydrogen bond-mediated mass transfer toward industrial water electrolysis. *Angew. Chem., Int. Ed.* **2025**, *64*, e202502151.

[52] Guo, Y. M.; Yu, Z. H.; He, B.; Chen, P. Z. Metallic cobalt mediated molybdenum nitride for efficient glycerol upgrading with water electrolysis. *Chin. Chem. Lett.* **2025**, *36*, 111010.

[53] Wu, Y. L.; Yu, Z. H.; Tong, Y.; Lin, C.; Zhang, N.; Chen, P. Z.

Interfacial bridge bonds induced strong electronic coupling of Co@V-WO_x catalyst for enhanced concurrent co-electrolysis performance. *Adv. Funct. Mater*., in press, https://doi.org/10.1002/adfm.202502104.

[54] Lin, C.; Lu, H. Y.; Ren, X. H.; He, B.; Peng, X.; Chen, P. Z. Long-term efficient electrosynthesis of adipic acid and hydrogen by heterostructural molybdenum-nickel alloy electrode. *Chem. Eng. J.* **2025**, *509*, 161475.

[55] Li, K. X.; Xie, B. B.; Feng, D. M.; Tong, Y. Ni_2Se_3–$CuSe_x$ heterostructure as a highly efficient bifunctional electrocatalyst for urea-assisted hydrogen generation. *ChemSusChem* **2022**, *15*, e202201656.

[56] Huang, T.; Gao, C.; Tong, Y.; Lu, X. L. Porous high-entropy oxide nanosheets as highly-efficient electrocatalysts for water oxidation. *Inorg. Chem. Front.* **2024**, *11*, 4179–4186.

[57] Feng, D. M.; Ren, X. H.; Tong, Y. Rational design of tungsten-doped cobalt molybdate nanosheet arrays for highly active ethanol-assisted hydrogen production. *Int. J. Hydrogen Energy* **2023**, *48*, 34244–34254.

[58] Li, K. X.; Tong, Y. Self-supporting nickel phosphide/ hydroxides hybrid nanosheet array as superior bifunctional electrode for urea-assisted hydrogen production. *ChemCatChem* **2022**, *14*, e202201047.

[59] Cheng, X. X.; Tong, Y. Hierarchical cobalt-nickel phosphide/molybdenum disulfide hybrid electrocatalyst triggering efficient hydrogen generation in a wider pH range. *ACS Appl. Energy Mater*. **2023**, *6*, 9577–9584.

[60] Li, K. X.; Feng, D. M.; Tong, Y. Hierarchical metal sulfides heterostructure as superior bifunctional electrode for overall water splitting. *ChemSusChem* **2022**, *15*, e202200590.

[61] Cheng, X. X.; Tong, Y. Interface coupling of cobalt hydroxide/molybdenum disulfide heterostructured nanosheet arrays for highly efficient hydrazine-assisted hydrogen generation. *ACS Sustain. Chem. Eng.* **2023**, *11*, 3219–3227.